

Nanoscale chemical mapping using three-dimensional adiabatic compression of surface plasmon polaritons

Francesco De Angelis^{1,2}, Gobind Das¹, Patrizio Candeloro², Maddalena Patrini³, Matteo Galli³, Alpan Bek⁴, Marco Lazzarino^{4,5}, Ivan Maksymov³, Carlo Liberale², Lucio Claudio Andreani³ and Enzo Di Fabrizio^{1,2*}

The fields of plasmonics, Raman spectroscopy and atomic force microscopy have recently undergone considerable development, but independently of one another. By combining these techniques, a range of complementary information could be simultaneously obtained at a single molecule level. Here, we report the design, fabrication and application of a photonic-plasmonic device that is fully compatible with atomic force microscopy and Raman spectroscopy. Our approach relies on the generation and localization of surface plasmon polaritons by means of adiabatic compression through a metallic tapered waveguide to create strongly enhanced Raman excitation in a region just a few nanometres across. The tapered waveguide can also be used as an atomic force microscope tip. Using the device, topographic, chemical and structural information about silicon nanocrystals may be obtained with a spatial resolution of 7 nm.

The development of spectroscopic techniques capable of physical and chemical mapping on a spatial scale of a few nanometres has been a topic of increasing interest in recent years. The rapid progress in new techniques has taken advantage of advances in another relatively new field—nanoplasmonics. Nanoplasmonics can be thought of as a ‘second youth’ for plasmonics, because the early studies in the field date back to the 1970s (ref. 1). This recent progress has been possible as a result of advances in nanofabrication technology. In fact, the characteristic length scale of the structures necessary to manipulate and generate surface plasmon polaritons (SPPs) in the visible and near-infrared region of the optical spectrum is in the nanometre regime^{2,3}. In this work, the minimum characteristic length scale of the proposed device is of the order of $\lambda/100$, where λ is the wavelength of the SPP exciting laser field.

The additional challenge of achieving complete control of light manipulation requires that the plasmonic architecture be designed in all three spatial directions. For this reason, conventional bidimensional fabrication methods derived from the microelectronics industry have had to be revised and improved to move beyond the planar ‘manhattan-like’ architectures characteristic of even the most advanced complementary metal oxide semiconductor (CMOS) technologies^{4,5}. Recent advances in this area have led to applications in subdiffraction imaging^{5,6} and nanobiosensing^{7–15}.

Nanoplasmonics and Raman spectroscopy

We describe the fabrication¹⁶ and demonstrate the first application of a device that, by combining different photonic concepts, materials and architectures, allows the generation of strongly localized SPPs to obtain a chemical map at the same spatial resolution (below 10 nm) of an atomic force microscope (AFM). The device consists of a two-dimensional dielectric photonic crystal cavity¹⁷

patterned on a Si_3N_4 AFM cantilever, together with a tapered silver waveguide placed at the centre of the cavity (Fig. 1a). The waveguide is a 2.5- μm -tall metallic cone, with a base diameter of 300 nm, and the minimum radius of curvature at the apex is controllable in the range 2.5–5 nm (Fig. 1c). The entire device is fabricated by means of ion milling and electron-beam induced deposition (see Methods and Supplementary Information). The device can be fully integrated with an inverted Raman microscope combined with an AFM stage, as shown in Fig. 1d.

The photonic crystal cavity enables an efficient coupling between the external laser source and the tapered waveguide, as shown by previous numerical simulations¹⁸ (see Supplementary Information), together with optimal sample illumination. In fact, the focal plane from which the SPPs are launched is 2.5 μm away from the cone apex where the Raman excitation is generated. This drastically lowers the background intensity at the sample plane. Thus, the spatial separation between SPP generation and Raman excitation efficiently increases the signal-to-noise ratio in the Raman spectrum. The focusing of SPPs follows an adiabatic compression mechanism, which causes a strong localization of the electrical field in a region with a size comparable to the apex radius of curvature^{19,20} (see Supplementary Information).

Another approach, in which SPP generation is efficiently obtained by direct illumination of a sharp conductive tip, is used in tip-enhanced Raman spectroscopy (TERS). This technique succeeds in achieving nanoscale chemical analysis with single molecule sensitivity^{21–25}. In conventional TERS experiments Raman scattering usually takes place at a diffraction-limited focal spot centred at the tip apex, which generates a far-field background superimposed on the TERS signal arising from the evanescent SPP field²⁶. In the present photonic-plasmonic device the Raman signal is generated only at the tip apex, with negligible background signal in the

¹Fondazione Istituto Italiano di Tecnologia (IIT), NanoBioScience Laboratory, via Morego 30, I16163 Genova, Italy, ²BIONEM Lab, University of Magna Graecia, Campus S. Venuta, Germaneto, viale Europa, I88100 Catanzaro, Italy, ³Department of Physics ‘A. Volta’ and UdR CNISM, University of Pavia, via Bassi 6, I27100 Pavia, Italy, ⁴CBM srl Area Science Park — Basovizza, I34012 Trieste, Italy, ⁵TASC National Laboratory, CNR-INFN, Area Science Park — Basovizza, I34012 Trieste, Italy. *e-mail: enzo.difabrizio@iit.it; difabrizio@tasc.infn.it

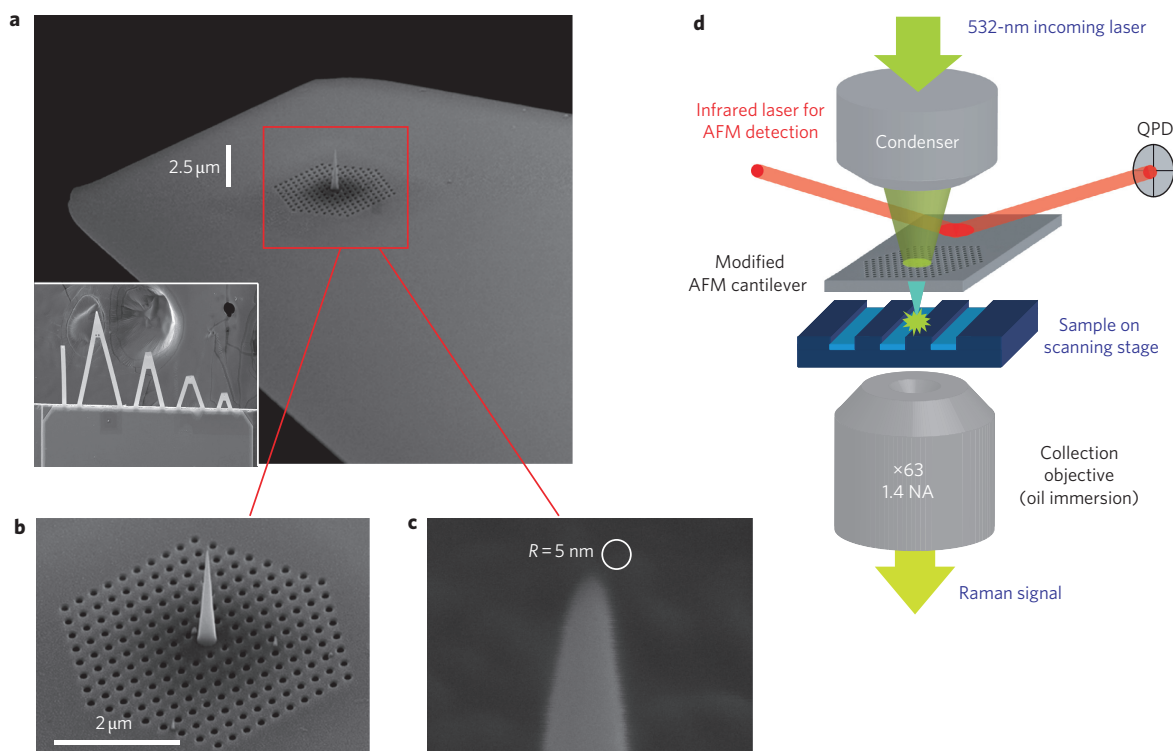


Figure 1 | Tapered waveguide on an AFM cantilever and experimental apparatus. **a**, Scanning electron microscope image of the device fabricated on a set of silicon nitride AFM cantilevers. The inset shows the whole chip with multiple tips. **b,c**, Close-up images of the photonic crystal cavity, fabricated on the silicon nitride membrane, and the tapered plasmonic waveguide with a conical shape and radius of curvature at the apex of 5 nm. **d**, Sketch of the experimental setup, showing the integration of the photonic-plasmonic device into an AFM-Raman microscope. The nanofabricated AFM tips and silicon nanocrystal sample are mounted on the AFM tip holder and on the sample stage, respectively (Nanowizard II, JPK Berlin). The AFM is equipped with a special module (TAO, JPK Berlin) that allows independent scanning of the tip or the sample in an area of $100 \times 100 \mu\text{m}^2$, with a scanning step resolution better than 1 nm. The sample and AFM tip can therefore be aligned independently with respect to one another and the optical axis of the microscope. AFM cantilever deflection is monitored through a conventional laser beam deflection system with an infrared laser ($\lambda = 860 \text{ nm}$) and detected by a four-quadrant photodiode (QPD). Raman and AFM laser spectral regions are separated and do not overlap.

far field. In addition, in the TERS configuration, the plasmonic coupling conditions are strongly dependent on the environment, sample characteristics and geometry. In the present device, however, the coupling is driven by the photonic crystal cavity, which is located far from the sample, and is much less sensitive to the above parameters.

To demonstrate that the excitation of the SPPs is due to the combination of the photonic crystal cavity and the tapered waveguide, and to exclude other focusing mechanisms, a direct comparison using different experimental conditions was carried out. We designed a specific experiment in which illumination was provided through a lens of numerical aperture (NA) equal to 0.2 and 25 mm working distance, and collection was realized by a $\times 150$ objective with NA = 0.95 with a focal plane that could be adjusted between different positions along the tapered waveguide (see Supplementary Information). We compared the complete device having both cone and cavity with those having a cone only and photonic crystal cavity only (Fig. 2a,b and c, respectively). The operating principle of the complete device is outlined in Fig. 2a. It can be seen that the progressive light is focused towards the apex of the waveguide. The spot size at the focal plane of the cone apex (Fig. 2a(iii)) is $\sim 350 \text{ nm}$ (diffraction-limited) and is much smaller than the illuminated region at the cavity plane (Fig. 2a(i)), indicating the generation and adiabatic focusing of SPPs towards the cone apex. When the cavity is absent (Fig. 2b), there is only divergent scattering from the bottom of the cone and no efficient generation and focusing of SPPs can be observed. In Fig. 2c, in the device with photonic crystal cavity only, there is

only a partial increase in intensity at the plane of the cavity, but no focusing can be detected out of this plane. This direct comparison demonstrates that the effectiveness of the coupling mechanism between the external laser and the tapered waveguide is due to the presence of the photonic crystal cavity. Numerical simulations that confirm the role of the photonic crystal cavity in the coupling mechanism are discussed in the Supplementary Information.

The SPP spatial confinement in the near field is comparable to the radius of curvature of the tapered waveguide apex, which in our best case lies between 2.5 and 5 nm. The expected electric field enhancement E due to adiabatic compression is theoretically evaluated for a silver cone by using the theoretical approach in refs 18 and 19. The enhancement E is defined as $E = |\mathbf{E}_{\text{tip}}|/|\mathbf{E}_{\text{base}}|$, where \mathbf{E}_{tip} and \mathbf{E}_{base} are the maximum electrical fields at the apex and bottom of the waveguide, respectively (see Supplementary Information). The calculated field enhancement as a function of radius of the curvature of the tip is reported in Fig. 3. Note that enhancement values of practical interest are in the range of 100. This value is reached when the radius of curvature of the tip is below 5 nm. For successful spectroscopy applications this necessitates state-of-the-art fabrication quality. The difficulty in fabricating three-dimensional tapered waveguides with this severe geometrical constraint highlights the importance of the experimental demonstration of three-dimensional adiabatic focusing in our device.

The architecture of the device and the mechanical stiffness of the tapered waveguide allow us to use it both as an AFM tip and as a nanometre light source for near-field Raman excitation. In other words, we are trying to obtain topographic and chemical mapping

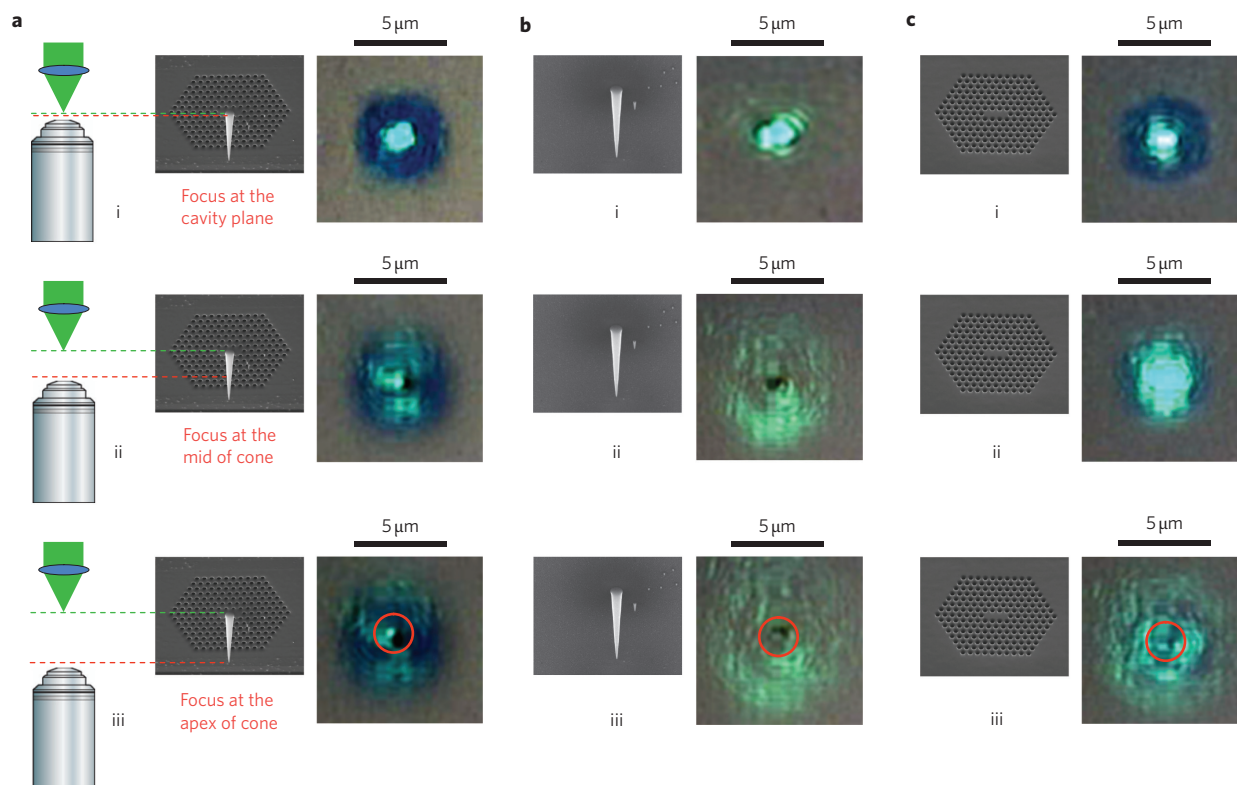


Figure 2 | Experimental test of SPP generation and propagation along the tapered waveguide. a–c, High-magnification optical microscope images of different devices under the same excitation conditions for the whole device (cone plus photonic crystal cavity) (a), the cone only (b) and the photonic crystal cavity only (c). Images are taken by focusing the excitation laser at the photonic crystal cavity plane (tapered waveguide base) with a NA = 0.2 lens and adjusting the focus of the imaging objective ($\times 150$, NA = 0.9) at three different positions along the vertical direction: (i) at the cavity plane (tapered waveguide base); (ii) at the mid height of the cone; (iii) at the apex of the cone.

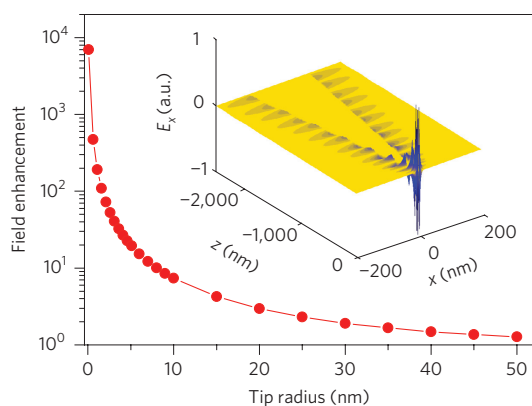


Figure 3 | Theoretical field enhancement in the plasmonic tapered waveguide. Calculated electric field enhancement as a function of the radius of curvature at the apex of the tapered waveguide. Inset: three-dimensional plot of the E_x radial component of the SPP field propagating along the tapered waveguide.

to yield structural and stress information with the same spatial resolution as is imposed by the geometry of the tip, that is, limited only by its radius of curvature. To accomplish this we first fabricated the device on an AFM cantilever. We then investigated a test sample for which the chemical composition had periodic spatial variations in the range of few nanometres. The test sample consisted of patches and gratings of silicon nanocrystals having different pitches (from several micrometres to a submicrometre scale) obtained by laser melting of a silica substrate previously fabricated by plasma-enhanced chemical vapour deposition (PECVD).

The average nanocrystal size was expected to be less than 10 nm (see Supplementary Information)²⁷. An AFM topography of a sample with submicrometre pitch is shown in Fig. 4.

Topographic and chemical mapping

Our experiments were performed using a home-built Raman AFM microscope (Fig. 1d) combining the three techniques of optical microscopy, Raman spectroscopy and AFM. Raman spectra were obtained in transmission configuration using a 532-nm solid-state laser providing a power of 1 mW to the sample. The photonic crystal cavity was illuminated from the top with a microscope condenser and a home-built lens system with NA = 0.35 and working distance of 70 mm. The scattered radiation was collected in the forward direction by a $\times 63$ oil-immersion objective with NA = 1.4 focused at the sample/tip plane. The radiation scattered by the sample was first filtered by a notch filter with an optical density of six and then analysed by a single-grating 750-mm focal length monochromator. Finally, Raman spectra were acquired using a high-sensitivity thermoelectric cooled electron-multiplied charge-coupled device detector. The acquisition time for each Raman spectrum was 100 ms.

To test the spatial resolution of our device for chemical mapping the best fabricated tapered waveguide with an apex radius of curvature of 2.5 nm was used. In this case, the expected theoretical field enhancement was ~ 100 (Raman enhancement $\sim 1 \times 10^8$). The AFM–Raman setup was operated in tapping mode and wet conditions (in distilled water) to measure simultaneously the topography and Raman intensity map by scanning the sample and acquiring Raman data across the lithographic structures, point by point. A three-dimensional map of the Raman signal at 520 cm^{-1} scanned over an area of $\sim 2,000 \times 20 \text{ nm}^2$ is shown in Fig. 5a. For this analysis

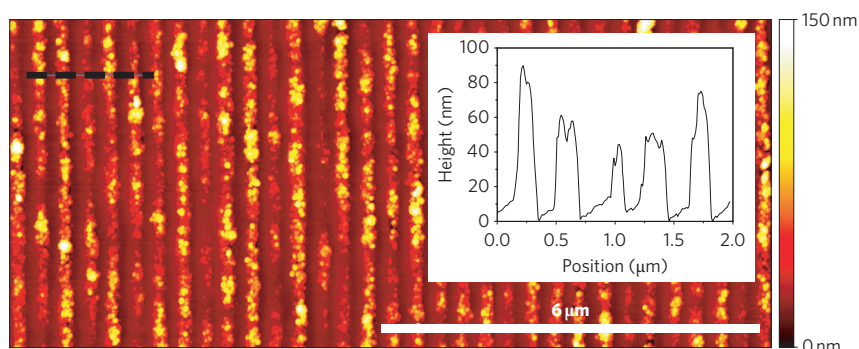


Figure 4 | AFM topography of the nanostructured sample. High-resolution image of Si/SiO_x sample with submicrometre pitch patterning with a periodicity of 500 nm, as shown in the inset. The height profile in the inset is measured along the dashed black line at the top-left corner in the image. The patterning is obtained by laser melting of a silica substrate (laser wavelength, 532 nm; power density, $\sim 2.5 \times 10^7$ W cm⁻²), producing trenches of silicon nanocrystals with a characteristic size of less than 10 nm.

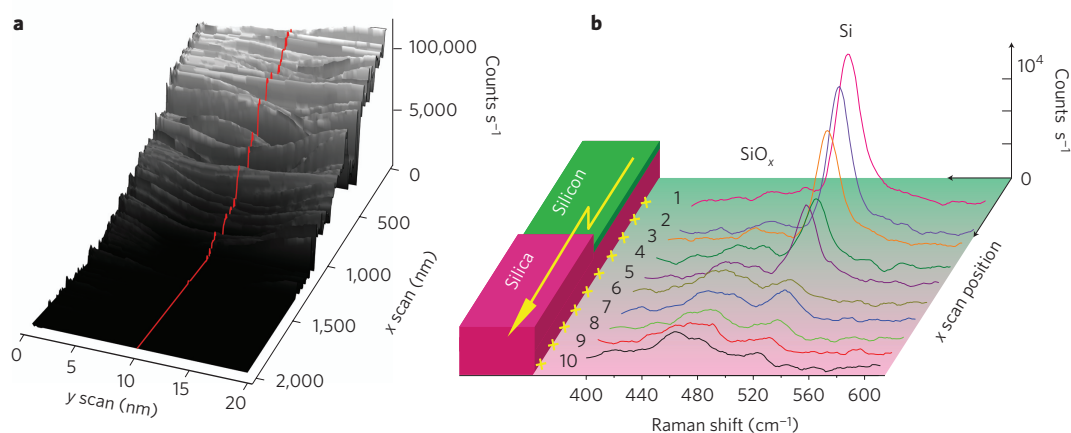


Figure 5 | Wide-scan Raman spectra and three-dimensional map of a silicon nanocrystal/SiO_x surface. **a**, Three-dimensional map of the Raman signal at 520 cm⁻¹ (c-Si phonon peak) from a representative scanning area across a silicon nanocrystal/SiO_x step boundary. **b**, Raman spectra measured from a representative line scan (red line along the three-dimensional map in **a**). Variations in the Raman spectra acquired from Position 1 (pink curve) to Position 10 (black curve) clearly reveal the corresponding variations of chemical composition from silicon (peak at ~ 520 cm⁻¹) to silica (peak at ~ 460 cm⁻¹). The AFM scan step size is 220 nm and the integration time for each single-point Raman spectrum is 100 ms.

we focused on the spectral range between 400 and 650 cm⁻¹. The spectral region between 430 and 480 cm⁻¹ is related to the presence of amorphous silica (SiO_x) and amorphous silicon. Although the Raman cross-section of silica is very low, our device can efficiently excite the Si–O bending vibration. The appearance on the spectrum of a peak centred at ~ 520 cm⁻¹ is evidence for the crossing of a crystallized silicon boundary. The continuous red line in Fig. 5a is a representative line scan for which the Raman spectral details are reported in Fig. 5b. Raman spectra were collected in the transmission configuration in the boundary region between the silica and the crystalline silicon (c-Si) region by scanning the sample with a step size of 220 nm. The corresponding Raman signal contrast at 520 cm⁻¹ is significant, with intensity ranging from 0 to 8,000 counts s⁻¹.

A more severe resolution test can be achieved by scanning the sample in a patterned region in which the crystalline and amorphous topography forms a grating with submicrometre pitch (Fig. 4). From the AFM measurements it could be seen that silicon, upon laser-induced crystallization, has its height reduced by ~ 100 nm, which results in the formation of a trench on the sample surface, as shown in the three-dimensional AFM map in Fig. 6a. The AFM scan step size was 7 nm. The red line in Fig. 6a is a representative AFM line scan from which we simultaneously obtained the Raman intensity map shown in Fig. 6b (upper

panel), in which the Raman spectrum extends from 504 to 540 cm⁻¹. The acquisition time of each Raman map was 5 s. Figure 6b (lower panel) shows the topography and Raman intensity for the same line scan. The Raman intensity is taken at the maximum of the silicon phonon peak at ~ 520 cm⁻¹.

The Raman intensity and relative peak amplitudes change from point to point, indicating an optical resolution of better than 7 nm. Point-by-point Raman measurements with up to 10 repetitions at the same position produced an average of $\pm 3.5\%$ signal error (Fig. 6b, lower panel). The capability of measuring this strong contrast in Raman intensity on a nanometre length scale is compatible with our experimental conditions only if the Raman excitation is caused, as theoretically expected, by a strongly localized SPP in a region comparable to the radius of curvature of the tapered waveguide apex. From the experimental data we estimated the experimental enhancement to be $E = 4.5 \times 10^6$ by comparing the silicon Raman intensity from a bulk crystalline sample with that from our sample when considering a scattering volume of ~ 70 nm³ ($2.5 \times 2.5 \times 10$ nm³, where 2.5 nm is the apex radius of curvature and 10 nm is the estimated *z* resolution for the tapered waveguide).

Nanoscale information from Raman spectra

These results were further reinforced by a quantitative analysis of the spectra obtained using the phonon confinement model

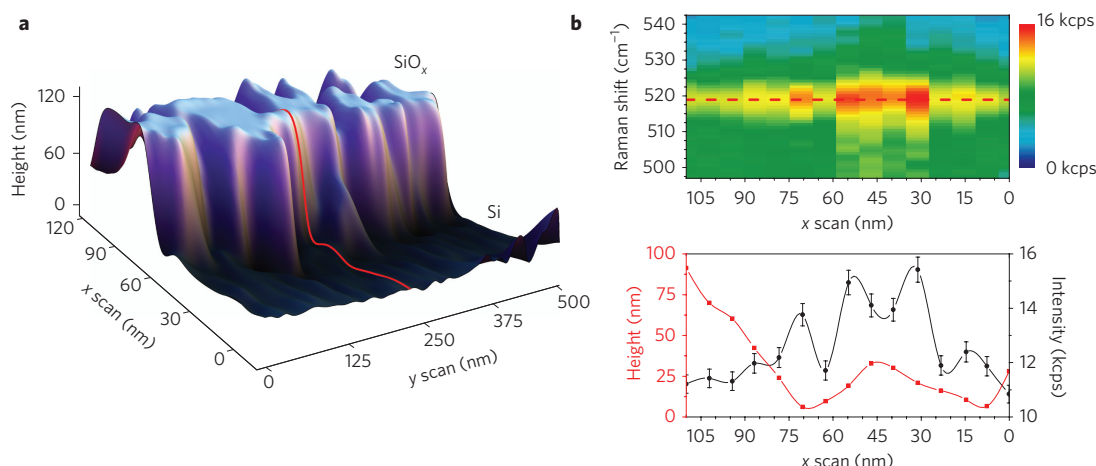


Figure 6 | High-resolution AFM and Raman mapping. **a**, AFM topography image across a submicrometre silicon nanocrystal/SiO_x trench. **b**, Raman intensity map (top panel) units of kilocounts per second, kcps, between 500 and 540 cm⁻¹, as measured simultaneously with AFM topography. The dotted red line corresponds to the red line scan in the topography map of **a**. The acquisition time of each Raman map is 5 s. Intensity (bottom panel) of the c-Si Raman peak at 520 cm⁻¹ (black dots, with error bars evaluated over 10 repetitions for each single position) and corresponding AFM line scan (red squares) along the red line scan of **a**. The scan step size is 7 nm.

(PCM)²⁸ adapted for size distribution^{29,30}. The model, through detailed lineshape analysis, allows the determination of crystalline grain size, crystalline fraction, nanocrystal stress conditions and their distribution in the amorphous matrix. The model assumes the relaxation of crystal momentum in the creation and annihilation of phonons in the nanocrystals³¹. Theoretical calculations to fit all experimental Raman data were made by considering that the phonon is strongly confined to the nanocrystals (see Supplementary Information). In this case, the phonon confinement function and its associated Fourier coefficient are $W(\mathbf{r}, L) = \exp(-8\pi^2 r^2/L^2)$ and $|C(0, \mathbf{q})|^2 \cong \exp(-(q^2 L^2/16\pi^2))$, respectively (where q is the wavevector in the Brillouin zone and L is nanocrystal lateral size).

Raman analysis for long scan measurements (220 nm step size, Fig. 5a,b) was carried out by using the PCM to evaluate silicon nanocrystal size. The Raman spectra show various bands in the 400–600 cm⁻¹ range. Vibrational bands at ~465 cm⁻¹ and ~515 cm⁻¹ are attributed to the convolution of SiO_x, amorphous silicon^{32,33} and silicon nanocrystals, respectively. Note that, in general, as the dimensions of the nanocrystal decrease, there is a redshift in the Raman vibrational frequency of silicon nanocrystals and an increase in bandwidth with respect to the c-Si band. The measured shift towards a lower frequency is due to the fact that the transitions with wavevector $q \neq 0$ become a factor when the silicon grain size decreases following the dispersion curve, $\omega(q) = 520.5 - 120(qa/2\pi)^2$, where $a = 5.43$ Å is the lattice constant. On the other hand, an increase in broadening is observed, because transitions other than $q = 0$ break the degeneracy of optical phonons, leading to additional transitions³¹. To estimate the size of the silicon nanocrystals, the band centred at ~520 cm⁻¹ was fitted using stress-corrected PCM (see Supplementary Information), whereas the vibrational band at ~470 cm⁻¹ was well reproduced by a Gaussian function. It can be seen that as we move from Position 1 to Position 10 in Fig. 5b, the intensity ratio of the Raman band centred at ~515 cm⁻¹ to the Raman band at ~465 cm⁻¹ decreases. Meanwhile, from PCM analysis, the size of silicon nanocrystals is found to increase from 41 to 56 Å, and, interestingly, size dispersion simultaneously increases. This effect could be due to a gradient heating of the SiO_x surface from the centre to the tail of the laser Gaussian beam during the melting process. In addition, the silicon Raman vibrational band at Positions 9 and 10 of Fig. 5b is observed at ~525 cm⁻¹. The Raman band shifts

towards higher wavenumbers with respect to the c-Si peak, revealing a strong compressive stress on the sample surface. We found that when the Raman signal of c-Si is intense (Position 1), there is a tensile stress of 0.2 GPa that redshifts the Raman band by 0.8 cm⁻¹ with respect to unstressed silicon. In moving from Position 1 to Position 10, the stress changes from tensile to compressive. This, very likely, is due to the Si-c melting in a SiO_x matrix through laser heating. The compressive stress observed at Position 10 is ~2 GPa (corresponding to a blueshift of 7.6 cm⁻¹; ref. 34).

The crystalline volume fraction from long scan measurements (Fig. 5a,b) was calculated by fitting the Raman spectra using various bands in the 400–490 cm⁻¹ and 500–520 cm⁻¹ ranges. Integrated Raman band intensity in the 400–490 cm⁻¹ range is attributed to an amorphous contribution, whereas for the crystalline contribution, bands in the 500–520 cm⁻¹ range are considered to be relevant. From Position 1 to Position 10 in Fig. 5b, a continuous decrease in crystalline fraction from 99% to 20% was measured (see Supplementary Information).

This analysis was further applied to a region of the sample with a submicrometre pitch, in which the AFM step size was 7 nm (Fig. 6). No spectral shift was observed in this case, but a variation in the c-Si/SiO_x ratio was clearly evaluated. The crystalline volume fraction was calculated at each point of the line scan as already explained. As can be seen from Fig. 6b, the Raman signal of the silicon nanocrystals decreases along the wall of the trench (scan position between 75 nm and 105 nm in Fig. 6b). In fact, in this region the submicrometre melting lithography causes a faster non-equilibrium recrystallization process. As a consequence, a sharp decrease in crystalline fraction of between 60 and 45% was measured when scanning from the centre of the trench to its wall. The experimental silicon Raman intensity map is in good agreement with the distribution of silicon nanocrystals estimated from PCM calculations (see Supplementary Information). The Raman intensity variations measured point by point with a step size of 7 nm were interpreted by the PCM analysis as being due to the grain size spatial distribution of the silicon nanocrystals, thus indicating the sub-10-nm resolution of our actual device. This confirms that the measured intensity variations in the Raman signal can be explained by the local generation of SPPs in a spatial region comparable to the size of the silicon nanocrystals.

In conclusion, the development of a photonic–plasmonic device that is fully compatible with AFM and Raman spectroscopy opens

up a number of significant opportunities in the nanoscale chemical mapping of materials. The approach could be of particular benefit in the nanoscale analysis of biological matter, such as in the investigation of cell membrane protein spatial distributions, in which chemical/physical bond strengths and amino acid composition *in vivo* conditions could be revealed. We believe that device architectures based on the adiabatic generation of SPPs have considerable potential for applications in which a reliable nanometre-sized light source is of utmost importance.

Methods

The whole device was fabricated using an FEI Nova Nanolab 600 dual beam system. The photonic crystal consisted of a triangular lattice of air holes (lattice constant = 250 nm, hole diameter = 160 nm) patterned on a 100-nm-thick Si₃N₄ membrane. Three missing holes in the centre generated a photonic crystal cavity, termed L3, tuned at $\lambda = 532$ nm. To fabricate the cavity on the AFM cantilever with a thickness of 100 nm, we thinned locally a commercially available Si₃N₄ cantilever (600 nm standard thickness) around the area of the photonic crystal cavity (for additional images and details see Supplementary Information). Ion-beam milling was then used to define the photonic crystal. A silver tapered waveguide was grown in the centre of the cavity using electron beam induced deposition from a gas precursor containing a platinum-carbon polymer (CH₃)₃Pt(C₆H₅)₃ (ref. 16). A thin film of silver was deposited on the surface of the device (30 nm thick), and then silver removed locally from the photonic crystal surface. The cone apex was machined with a radius of 2.5–5 nm using low-current ion milling (current, 10 pA). Finally, the sample was immersed in diluted fluoride acid for a few seconds to remove a 10-nm layer of silicon nitride implanted by gallium during the milling process.

Received 14 May 2009; accepted 16 October 2009;
published online 22 November 2009

References

1. Raether, H. *Surface Plasmons* (Springer, 1988).
2. Masuhara, H. & Kawata, S. (eds) *Nanoplasmonics* Vol. 2 (Elsevier, 2006).
3. Murray, W. A. & Barnes, W. L. Plasmonic materials. *Adv. Mater.* **19**, 3771–3782 (2007).
4. Kino, G. Tuning into optical wavelengths. *Nature Photon.* **2**, 210–211 (2008) and references therein.
5. Zheludev, N. I. What diffraction limit? *Nature Mater.* **7**, 420–422 (2008).
6. Zhang, X. & Liu, Z. Superlenses to overcome the diffraction limit. *Nature Mater.* **7**, 435–441 (2008).
7. Anker, J. N. *et al.* Biosensing with plasmonic nanosensors. *Nature Mater.* **7**, 442–453 (2008).
8. Barnes, W. L., Dereux, A. & Ebbesen, T. W. Surface plasmon subwavelength optics. *Nature* **424**, 824–830 (2003).
9. Prodan, E., Radloff, C., Halas, N. J. & Nordlander, P. A hybridization model for the plasmon response of complex nanostructures. *Science* **302**, 419–422 (2003).
10. Verhagen, E., Kuipers, L. & Polman, A. Enhanced nonlinear optical effects with a tapered plasmonic waveguide. *Nano Lett.* **7**, 334–337 (2007).
11. Taminiau, T. H., Stefani, F. D., Segerink, F. B. & Van Hulst, N. F. Optical antennas direct single-molecule emission. *Nature Photon.* **2**, 234–237 (2008).
12. Merlein, J. *et al.* Nanomechanical control of an optical antenna. *Nature Photon.* **2**, 230–233 (2008).
13. Zenobi, R. Analytical tools for the nano world. *Anal. Bioanal. Chem.* **390**, 215–221 (2008).
14. Gerhardt, I. *et al.* Scanning near-field optical coherent spectroscopy of single molecules at 1.4 K. *Opt. Lett.* **32**, 1420–1422 (2007).
15. Hartschuh, A., Pedrosa, H. N., Novotny, L. & Krauss, T. D. Simultaneous fluorescence and Raman scattering from single carbon nanotubes. *Science* **301**, 1354–1356 (2003).
16. Di Fabrizio, E. *et al.* Procedimenti di fabbricazione di un dispositivo a cristallo fotonico provvisto di guida d'onda plasmonica. Italian patent TO2008A000693 (2008).
17. Andreani, L. C. & Gerace, D. Photonic crystal slabs with a triangular lattice of triangular holes investigated using a guided-mode expansion method. *Phys. Rev. B* **73**, 235114 (2006).
18. De Angelis, F. *et al.* Hybrid plasmonic-photonic nanodevice for label-free few/single molecule detection in the far field. *Nano Lett.* **8**, 2321–2327 (2008).
19. Stockman, M. I. Nanofocusing of optical energy in tapered plasmonic waveguides. *Phys. Rev. Lett.* **93**, 137404 (2004).
20. Babadjanian, A. J., Margaryan, N. L. & Nerkararyan, V. Superfocusing of surface polaritons in the conical structure. *J. Appl. Phys.* **87**, 3785–3793 (1999).
21. Anderson, M. S. Locally enhanced Raman spectroscopy with an atomic force microscope. *Appl. Phys. Lett.* **76**, 3130–3133 (2000).
22. Hayazawa, N., Inouye, Y., Sekkat, Z. & Kawata, S. Metallized tip amplification of near-field Raman scattering. *Opt. Commun.* **183**, 333–336 (2000).
23. Stöckle, R. M., Suh, Y. D., Deckert, V. & Zenobi, R. Nanoscale chemical analysis by tip-enhanced Raman spectroscopy. *Chem. Phys. Lett.* **318**, 131–136 (2000).
24. Hartschuh, A., Sanchez, E. J., Xie, X. S. & Novotny, L. High-resolution near-field Raman microscopy of single-walled carbon nanotubes. *Phys. Rev. Lett.* **90**, 095503 (2003).
25. Hu, D. H., Micic, M., Klymyshyn, N., Suh, Y. D. & Lu, H. P. Correlated topographic and spectroscopic imaging by combined atomic force microscopy and optical microscopy. *J. Lumin.* **107**, 4–12 (2004).
26. Anderson, N., Anger, P., Hartschuh, A. & Novotny, L. Subsurface Raman imaging with nanoscale resolution. *Nano Lett.* **6**, 744–749 (2006).
27. Mchedlidze, T. *et al.* Light-induced solid-to-solid phase transformation in Si nanolayers Si–SiO₂ multiple quantum wells. *Phys. Rev. B* **77**, 161304 (2008).
28. Richter, H., Wang, Z. P. & Ley, L. The one phonon Raman spectrum in microcrystalline silicon. *Solid State Commun.* **39**, 625–629 (1981).
29. dos Santos, D. R. & Torriani, I. L. Crystallite size determination in μ c–Ge films by X-ray diffraction and Raman line profile analysis. *Solid State Commun.* **85**, 307–309 (1993).
30. Kohno, H., Iwasaki, T., Mita, Y. & Takeda, S. One-phonon Raman scattering studies of chains of crystalline-Si nanospheres. *J. Appl. Phys.* **91**, 3232–3235 (2002).
31. Fauchet, P. H. & Campbell, I. H. Raman spectroscopy of low dimensional semiconductors. *Crit. Rev. Solid State Mater. Sci.* **14**, S79–S101 (1988).
32. Rojas, S., Zanolli, L., Borghesi, A., Sasella, A. & Pignatelli, G. U. Characterization of silicon dioxide and phosphosilicate glass deposited films. *J. Vac. Sci. Technol. B* **11**, 2081–2089 (1993).
33. Daldosso, N. *et al.* Silicon nanocrystal formation in annealed silicon-rich silicon oxide films prepared by plasma enhanced chemical vapor deposition. *J. Appl. Phys.* **101**, 113510 (2007).
34. Khriachtchev, L., Rasanen, M. & Novikov, S. Laser-controlled stress of Si nanocrystals in a free-standing Si/SiO₂ superlattice. *Appl. Phys. Lett.* **88**, 013102 (2006).

Acknowledgements

This work was funded under European Project DIPNA FP6-STREP proposal no. 032131, Project SMD FP7-NMP 2800-SMALL-2 proposal no. CP-FP 229375-2, MIUR-PRIN2008 project—Italian Ministry of University and Research, FIRB contract no. RBAP06L4S5, Fondazione Cariplo project 2007-5259, and project POSEIDON under POR Calabria 2006-2008. M.L. and A.B. acknowledge funding from FP6-BINASP-SSA011936 project.

Author contributions

All authors contributed significantly to the work presented in this paper.

Additional information

The authors declare no competing financial interests. Supplementary information accompanies this paper at www.nature.com/naturenanotechnology. Reprints and permission information is available online at <http://npg.nature.com/reprintsandpermissions/>. Correspondence and requests for materials should be addressed to E.D.F.